ELEMENTS OF

Optical and Laser Beam Scanning

Modeling of Mirror and Prism Scanning Devices

Yajun Li

SPIE PRESS
Bellingham, Washington USA

Library of Congress Control Number: 2021938746

Published by
SPIE
P.O. Box 10
Bellingham, Washington 98227-0010 USA
Phone: +1 360.676.3290
Fax: +1 360.647.1445
Email: books@spie.org
Web: www.spie.org

Printed in the United States of America.
First Printing.
For updates to this book, visit http://spie.org and type “PM331” in the search field.

Dedicated to the memory of my mother, Professor Yujun Luo;
my father, Professor Hen Li; and my wife, Hui-Tse Li.

Contents

Preface

Scanning technology for optical and laser systems is used in the controlled deflection of optical and laser beam for information transfer, such as actively or passively detecting events in a given direction (e.g., lidar), detecting information from a given surface (e.g., bar-code scanning) or inducing a physical effect (e.g., photoconductivity or photomagnetism) on the surface during a flying spot scan. All of these scanning systems have been applied to a number of useful products that have a direct bearing on our life.

The scope of this book is restricted to mirror scanning systems and rotating wedge prism scanning systems. Here, "mirror" means a plane reflecting surface, and "wedge" means a thin prism with a right triangle cross-section.

Over nearly 30 years, I have been interested in the mathematical analysis of scanning devices for optical and laser systems to yield results with higher accuracy than those obtained from geometrical construction of imaging of an object by a movable mirror or prism, which was a method to yield design data for scanning devices engineering when mathematical model is difficulty to obtain from open publications, in which the exact form of important equations may be considered as proprietary.

My analytical results have been summarized according to the format of original research papers, most of which were written solely by me and published in archival journals. After their publication, I usually received emails from readers with questions, friendly comments and reprints requests. This situation was different from my experience acquired after publishing theoretical papers on diffraction and coherence of light in optical physics, although many of them have high citation numbers over a longer period of time. Reader reactions to my research encouraged me to prioritize this book as a summary of the results I obtained in the past.

I appreciated the opportunity that SPIE gave me to collect my published and unpublished manuscripts together, along with detailed commentary and corrections in a book so that readers need not search through old journals. Readers of this book are assumed to have a foundation in vector operation and calculus, and a reasonable knowledge of elementary optics and laser. Detailed proofs that require long derivations are sometimes omitted but can be found in either the appendices or the cited references.

This book is divided into three parts, starting with an introductory chapter for the laws of reflection and refraction and the mathematical preliminaries of analytical raytracing (most expressions are in vector forms). Chapters 2 through 4 are the first part, which covers topics of mirror scanning devices with one axis of rotation for conic-sections scanning. Chapters 5 through 6 are the second part, which covers topics of mirror scanning devices with two axes of rotation, e.g., gimbaled mirror and Galvanometric scanners in cascade for two-dimensional scanning. Chapters 7 through 10 are in the third part to address Risley-prism-based beam-steering systems (i.e., rotating wedge prism scanning systems) with two to three elements for moving target searching and tracking.

Since each chapter in this book is an enlarged version of my technical paper focused on a specific topic as noticed by a single line about the main reference material of that topic at the beginning of each chapter, which may be helpful to readers who are interested in a specific scanning device and want to know its analytic model and computed results.

Writing a book is time-consuming and laborious; I doubt that many books have been written without some substantial help and encouragement by others. This book is no exception; therefore, I wish to express my appreciation to my friends at Symbol Technologies, Inc., especially Dr. Jerome Swartz and Dr. Satya Sharma.

I am obliged to SPIE Press, specifically, Dr. Eugene Arthurs, who initiated this project, and Mr. Scott McNeill, who helped bring it to fruition. I am also obliged to the Optical Society for permission to reproduce drawings from my papers published in the *Journal of Optical Society of America A* and *Applied Optics*. I thank my sister, Professor Xiaoyu Li; my niece, Lily Ji; and my friend, Earl O'Neil—without their encouragement and support, this book would not have been possible.

Yajun Li
October 2021

Chapter 1
Introduction

1.1 Brief History

Laser-beam-scanning systems can be divided into two categories: (1) angular-scanning systems and (2) linear or curvilinear translation-scanning systems. The subject of scanning in these two basic processes of scanning actions is often viewed quite differently, e.g., the first type is suitable for detecting events (in an active or passive way) in a given direction (e.g., lidar for remote sensing), and the second type is suitable for detecting information from a given surface or inducing a physical effect (such as photoconductivity or photomagnetism) on the surface during a flying spot scan. All these scanning systems have been applied to a number of useful products (Refs. [1.1]–[1.5]). For example, people today are familiar with the use of optical scanners: the laser- or LED-based barcode scanners found at the checkout counters in every retail store.

Reflection in an optical system containing immovable plane mirrors is a subject with a long history that can be traced back to the research of Smith (Ref. [1.6]) in the early part of the last century. The basic principles are now quite well understood and have been summarized in an optical handbook by Levi (Ref. [1.7]) and in a book chapter by Hopkins (Ref. [1.8]). For systems containing scanning mirrors, some theoretical but mainly practical and heuristic considerations have been introduced, elaborated, and summarized by Beiser (Refs. [1.1], [1.2] and [1.9]), Marshall (Ref. [1.10]), Sherman, (Refs.[1.2] and [1.11]), and many others (Refs. [1.12] and [1.13]) in the form of journal papers, monographs, book chapters, conference papers, and industrial patents.

This chapter is divided into three sections. First, we review the historical development of modeling mirror-scanning devices and then consider the vector expressions of the laws of reflection and refraction that laid the foundation of scanning of light beams. These laws describe some of the basic relationships when the light travels from one medium to another. In the applications of the law of reflection, one needs to know the point on the rotating mirror where the ray of incidence hits it and is then reflected. Vector expression of the location of the point of ray−mirror intersection is derived in the second section.

the position vector $\mathbf{r}_{k-1}$. The ray reflected off the mirror M_{k-1} is in the direction specified by the unit vector $\hat{\mathbf{s}}_{k-1}^{(r)} = \hat{\mathbf{s}}_k^{(i)}$, and then this ray strikes the mirror M_k at the point Q_k specified by the position vector $\mathbf{r}_k$. Evaluation of $\mathbf{r}_k$ is essential for raytracing, and it can be found from the definition of ray direction vector, given by

$$\hat{\mathbf{s}}_k^{(i)} = \frac{\mathbf{r}_k - \mathbf{r}_{k-1}}{|\mathbf{r}_k - \mathbf{r}_{k-1}|}; \tag{1.6a}$$

rearranging the terms leads to

$$\mathbf{r}_k = \mathbf{r}_{k-1} + |\mathbf{r}_k - \mathbf{r}_{k-1}|\hat{\mathbf{s}}_k^{(i)} \quad \text{or} \quad \hat{\mathbf{s}}_k^{(i)} \times (\mathbf{r}_k - \mathbf{r}_{k-1}) = 0. \tag{1.6b}$$

Since Q_k is a point on the reflective surface of plane mirror M_k, which implies that $\mathbf{r}_k$ satisfies the equation for the planar mirror surface, i.e.,

$$\mathbf{r}_k \cdot \hat{\mathbf{n}}_k = p_k, \tag{1.7a}$$

where $\hat{\mathbf{n}}_k$ is the unit vector normal to the mirror M_k, and p_k is the perpendicular distance from the origin O of the coordinate system to M_k. After substituting Eq. (1.6b) into Eq. (1.7a), we find that

$$p_k = \mathbf{r}_k \cdot \hat{\mathbf{n}}_k = (\mathbf{r}_{k-1} + |\mathbf{r}_k - \mathbf{r}_{k-1}|\hat{\mathbf{s}}_k^{(i)}) \cdot \hat{\mathbf{n}}_k. \tag{1.7b}$$

Solving Eq. (1.7b) for $|\mathbf{r}_k - \mathbf{r}_{k-1}|$ yields

$$|\mathbf{r}_k - \mathbf{r}_{k-1}| = \frac{p_k - \hat{\mathbf{n}}_k \cdot \mathbf{r}_{k-1}}{\hat{\mathbf{n}}_k \cdot \hat{\mathbf{s}}_k^{(i)}}. \tag{1.8}$$

Again, after substituting from Eq. (1.8) into Eq. (1.6b), the position vector for the ray and mirror intersection is expressible in the recurring form

$$\mathbf{r}_k = \mathbf{r}_{k-1} + \frac{p_k - \hat{\mathbf{n}}_k \cdot \mathbf{r}_{k-1}}{\hat{\mathbf{n}}_k \cdot \hat{\mathbf{s}}_k^{(i)}} \hat{\mathbf{s}}_k^{(i)}. \tag{1.9}$$

Note that p_k in the above equations is not always positive, and we may replace p_k in Eq. (1.9) with $\mathbf{r}_k \cdot \hat{\mathbf{n}}_k$ in mathematical manipulations to guarantee the correctness of the computed results.

1.3 Scan Fields and Scan Patterns

This section considers reflections in systems containing multiple rotary mirrors, wherein the scanning mirror can rotate either continuously or reciprocally depending on the control law, i.e., constraints imposed on mirror motion and on the drive functions [see the definition of mirror drive functions

scan center, where the vertex of the cone is located and the half-vertex angle is a measure of the rate of cone broadening. It can be expressed as

$$\mathrm{U} = \arccos(\hat{\mathbf{s}}_N^{(r)} \cdot \hat{\mathbf{e}}_{\mathrm{ax}}), \tag{1.21}$$

where $\hat{\mathbf{e}}_{\mathrm{ax}}$ is the unit vector of the axis of the cone. In the case of single origin scanning, as shown in Fig. 1.5, we may define the beam scan angle as

$$\mathrm{DA} = \arccos(\hat{\mathbf{s}}_N^{(r)} \cdot \hat{\mathbf{e}}_{\mathrm{ref}}), \tag{1.22a}$$

where $\hat{\mathbf{e}}_{\mathrm{ref}}$ is the unit vector of the reference axis (i.e., the base line) to measure the angle DA, the extreme values of which determine the extension of scan field.

Furthermore, the angular transfer function ATF, i.e., the ratio of the optical to mechanical scan angles or the angular magnification of mirror scanning system, is defined by

$$\mathrm{ATF} = \mathrm{DA}/\theta,$$

For the common case of mirror scanning, the beam deflection angle $\mathrm{DA} = 0$ at the point when mirror rotation angle $\theta = 0$; to avoid uncertainty and to give an approximate expression for small scan angle θ, the angular transfer function ATF may be further expressed as

$$\mathrm{ATF} = \lim_{\theta \to 0}(\mathrm{DA}/\theta). \tag{1.22b}$$

Note that DA defined above is different from the angle shown by the symbol Θ in Fig. 1.5, which is a measure of the angular motion of scanning spot along the scan pattern on the observation plane, which can be expressed as

$$\Theta = \arctan(n_N^{(r)}/m_N^{(r)}). \tag{1.23}$$

Equations (1.22a) and (1.23) may predict identical results under certain conditions.

1.3.3 Optical distortions in scan patterns

The scan-line bow (SLB) is a parameter used to measure scan-line curvature as illustrated in Fig. 1.6, in which ΔH represents the bow and

$$\mathrm{SLB} = 100\frac{\Delta H}{L}(\%), \tag{1.24}$$

where L is the length of the scan line. The SLB becomes an irrelevant parameter when a straight-line scan is not desirable.

Chapter 2
One-Mirror and One-Axis Scanning Devices

To give a unified treatment for one-mirror and one-axis scanning systems of different configurations, a single-facet scanner [see Fig. 2.1(a)] is selected as the model scanner, from which one may gain some insight about the structures of scan field and scan pattern and their variations. Some of the expressions derived for model scanners are general formulas that can be revised to describe the scan field between mirrors in multi-mirror scanning systems.

Since the model scanner is a one-mirror and one-axis scanning device, the serial number for the characterization parameters of the scanner will not be shown in the analysis.

The main references of this chapter are [2.1] and [2.2]

2.1 Single-Facet Model Scanner

A single-facet scanner is a simple mechanical scanner, in which a mirror rotates at an end of a motor shaft when the mirror is inclined at an angle γ to the axis of mirror rotation, as shown in Fig. 2.1(a). Due to this configuration, a single-facet scanner is also known as a cantilevered scanner or a monogonal scanner because it may be regarded as a special case of the pyramidal polygon scanner when the number of facets reduces to one [see, e.g., Section 3.4].

In this section, we consider a perfect monogon scanner, i.e., no random error sources affect the mirror performance, no shaft wobble, and so on.

2.1.1 Scanning geometry and the acceptance angle of the ray of incidence

The scanning geometry (i.e., the shape, size and relative opto-mechanical arrangements) of a single-facet scanner together with a standard right-hand Cartesian coordinate system are shown in Figs. 2.1(a) and (b), in which the angular position of the rotating mirror and direction of the ray of incidence to

This expression becomes invalid when $|\cot\gamma\cot\phi| > 1$, which implies the beam of incidence may hit the mirror reflective surface for a complete rotation period. This situation allows us to develop Eq. (2.3) analytically, because $|\cot\gamma\cot\phi| > 1$ can be further expressed as

$$|\tan\phi| < |\tan(90^\circ - \gamma)|, \quad \text{or} \quad \phi < 90^\circ - \gamma.$$

As a numerical example, consider a system of mirror inclined angle $\gamma = 45°$ and incident beam tilted angle $\phi = 60°$ (note, $\phi > \phi_{\max} = 90° - 45° = 45°$), then we obtain

$$\theta_C = \arccos(-\cot 60^o \cot 45^o) = \arccos(-1/\sqrt{3}) = \pm 125.3^o,$$

which implies no scan pattern can be displayed on the observation plane when the mirror rotation angle θ is between $+125.3°$ and $+234.7°$, which is $\sim 30\%$ of a complete rotation period. In the remainder of this section, we assume the angle of incidence $\phi < \phi_{\max,}$ i.e., the beam of incidence can hit the mirror surface for a complete rotation period.

2.1.2 Single-origin scanning

The scanning system shown in Fig. 2.1(b) is symmetric with respect to the xz plane, which may be regarded as the meridional plane of the scanning system. On this plane are the axes of mirror rotation and beam of incidence, which are reference lines that define the structural parameters of the scan field, such as

- The maximum angular extension of the scan field: The axes of beams of incidence and reflections at mirror rotation angles $\theta = 0°$ and $180°$ are co-planar and the angle included between beams reflected at $\theta = 0°$ and $180°$ represents the maximum angular extension of the scan field as shown by the symbol $2U_m$ in Figs. 2.2(a)–(c) for the scan fields produced by systems of different angle of beam incidence $\gamma < 45°$, $= 45°$, and $> 45°$, respectively.
- Observation plane for scan pattern display: Angle $2U_m$ is equally divided by the axis Oz' that makes an angle ϕ to the z axis, the same angle as the incident beam made with the z axis. Axis Oz' is selected as the Z axis of the observation plane at a distance P from the origin O of the coordinate system.
- The vertex angle of the scan field: Because the point of incidence is a fixed point on the axis of mirror rotation, the scan field has a single origin (i.e., the center of the scanning beams) that is the vertex of a cone formed by the axes of scanning beams. The angle $U_m = 2\gamma$ represents the maximum value of the half-vertex angle as shown in Fig. 2.2(a). U_m depends solely on the mirror inclined angle γ, and $2U_m = 180°$

"Observation Plane II" in the lower part of Fig. 2.14(a). This curved scan line can be expressed as

$$X = (P - x_0)\tan\theta \quad \text{and} \quad Y = -x_0\cos\theta. \tag{2.23}$$

Scan-line bow (SLB) defined in Eq. (1.24) is one of the optical distortions in association with this scan pattern, which can be expressed as

$$\text{SLB} = 50 \times \frac{x_0}{P - x_0}\tan(\theta/2)\cos(\theta)(\%). \tag{2.24}$$

Also, the scan velocity is not constant across the scan path, and the scan linearity (LIN) defined in Eq. (1.25b) is given by the formula

$$\text{LIN} = 200 \times \left\{1 + \left[\frac{1}{\cos^4\theta} + \left(\frac{x_0}{P - x_0}\right)^2 \sin^2\theta\right]^{1/2}\right\}^{-1}(\%), \tag{2.25}$$

which reduces to Eq. (2.8) in the far-field scanning, i.e., when $P >> x_0$.

2.2 Galvanometer-Based Scanner and Conic-Section Scan Patterns

A vector approach of analytic ray-tracing has been developed and applied to a single-facet scanning device that was selected as the model scanner to unify the techniques and methods in the structural analysis of the scan fields produced by one-mirror and one-axis scanning systems of different configurations. This section considers applications of the results of the model scanner presented in Section 2.1 to explore the distinctive features of the following one-mirror and one-axis scanning devices:

- Galvanometric scanner,
- Paddle scanner, and
- Golf-club scanner.

Here, the Galvanometric scanner (or, Galvo, in short) is a Galvanometer-driven laser scanning mirror that can produce a scan field in the shape of a right-circular cone with its vertex at the center of the mirror. Because of this, the scan pattern on the plane of observation can only be one of the following conic sections:

- Ellipse (a circle is considered as a type of ellipse),
- Parabola, and
- Hyperbola.

The final result depends on the position and orientation of the plane in cutting the cone.

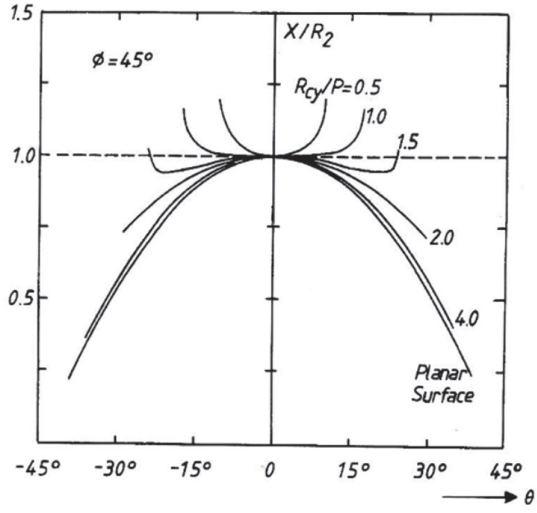

Figure 2.30 Scan patterns produced by a Galvanometric scanner with non-normally incident light projecting onto cylindrical surfaces with different radii of curvature R_{cy}.

The square root must be positive, and we obtain

$$\tan\phi < \frac{R_{CY}}{\sin 2|\theta_m|\sqrt{P(P+2R_{CY})}},$$

where θ_m is the amplitude of mirror rotation. Figure 2.30 is a plot of Eq. (2.57a) to show the prediction of scan pattern on the cylinder. In this plot, $R_2 = (P\tan\phi)$ and it is seen that the scan line bowed toward the scanning mirror for small-radius cylinders and to the opposite side for large-radius cylinders.

2.3 Shaft Encoders and Digital Galvanometric Scanner

A rotary encoder, also known a shaft encoder, is an electro-mechanical device that converts the angular position or motion of a shaft to an electrical signal, which provides the foundation of digitalizing one-mirror and one-axis scanners and systems built up by their combinations, such as the XY scanners and the three-dimensional scanners.

There are numerous types of encoders and they can be categorized from their respective special characters. For example [2.9, 2.10],

- According to the method of aquring position information of a movable mirror, there are three main types: optcal encoder, magnetic encoder and resolvers.

- Absolute position is measured immediately when the system is switched on and, therefore, no counter and home base are needed.
- Using reflected binary code in which one bit changes at a time, which reduces encoder communication errors.

However, the incremental optical rotary encoder is less complex than its absolute counterpart, thus typically less expensive.

To reduce the complexity in disk pattern and enlarge the through-hoe in its center, in the meantime, keep technical specifications of absolute encoder, a new encoder, called the pseudorandom encoder has been developed for measuring linear or angular distance and finding position. Pseudorandom in this description means disk pattern that is designed according to pseudorandom sequences of numbers which are difficult to predict and exhibits statistical behavior similar to truly random sequences. [2.22]

The pseudorandom encoder is different from the conventional absolute encoder in its disc pattern, which has a uniformly distributed notch design just as an incremental encoder to measure distance. A second track of code is used to find the position just like an absolute encoder; however, an absolute encoder tells position from reading from multiple parallel tracks while a pseudorandom encoder uses one single track. This feature allows pseudorandom rotary encoders to have smaller diameters and larger through-holes. To know its position, the encoder must first move a certain distance to read the code, because the algorithm for generating pseudorandom sequences needs a "seed" to start iterative computations. The distance is generally small, about 1-2 degrees for rotary encoders and 1 mm for linear encoders, though this mode of behavior does create difficulties in some applications since position is not immediately known when the system starts. [2.23]

2.3.3 Digital Galvanometric scanners

It is interesting of noting there is no Galvanometer in a digitized Galvanometric scanner if we compare the configurations shown in Fig. 2.16(a) and Fig. 2.35. In conventional configuration Galvanometer is the actuator to drive mirror for laser beam scanning along a straight of curved path with lower accuracy and precision, whereas the digital Galvanometric scanners are motorized mirror mount for laser beam steering or scanning and can direct laser beam to target with high accuracy and precision by the way of real-time closed loop mirror position control.

Nowadays digital Galvanometric scanners can be found wherever laser beams are used for materials processing, laser light shows, manufacturing, packaging, cutting, marking, welding, and numerous other applications.

The closed loop control system formulas are implemented in computer language in the form of software, which performs the calculations required by the governing equations of mirror motion (see, e.g., Equations in Table 2.3)

Chapter 3
Scan Field of Rotating Reflective Polygons

Polygonal scanners are rotating-prism scanning devices for laser beam scanning. The primary advantages of the polygonal scanners are scan speed, the availability of wide scan angles, fast retrace times, and velocity stability.

There are four types of regular polygons: prismatic, pyramidal, and their inverted versions. [1.1, 3.1, 3.2] However, the equations derived for the model scanner, i.e., for the single-facet scanning devise or monogonal scanner (see Section 2.1), can be readily extended to pyramidal and inverted polygons. [3.4, 3.5]

The geometrical relationships characterizing the behavior of polygon scanners have been discussed in many open publications, and Refs. [1.1, 1.3–1.5, 1.9, 1.11; 3.1–3.9] constitute a partial list of them to provide initial insights into the polygon-scanning systems that will be described in this chapter.

This chapter may be regarded as an application of the general theory of laser beam scanning by rotary mirrors outlined in Chapters 1 and 2 to an analysis of the light distribution in the scan field produced by a rotating polygon scanner. Some special topics, but ones that are important in practicality, are discussed in greater detail within the accuracy of ray optics. They include the scan duty cycle, the locus of the scan center, the depth of the scan field (i.e., the region of scan center displacement along the optical axis), the lines of force in the scan fields produced by prismatic polygons of different sides, and the scan patterns produced by convergent beam scanning.

This chapter is divided into four sections.:

- Section 3.1 develops and illustrates the notation, terms, and conditions of the geometrical relationship characterizing the behavior of the scan field produced by a prismatic polygon scanner.

the incoming ray to pass beyond the edge of the scan lens housing. The requirement of $\gamma > 0$ can also be expressed in the form

$$(x_0/R_T)\sin\psi > \sin(\Theta_p/2) \text{ or } 2x_0\sin\psi > W. \tag{3.18}$$

3.2.3 Scanning geometry for symmetric scan field distributions

Equation (3.16) predicts that there exists a special case relating to a symmetric scan field distribution when $AS = 0$, i.e., when $\Delta\theta = 0$. After substituting from $\Delta\theta = 0$ in Eq. (3.15), we arrive at the equation

$$[(x_0/R_T) - 1]\sin\psi = 0, \tag{3.19}$$

which implies two possibilities to produce a symmetric scan field distribution:

1. $\psi = 0$: The ray of incidence is parallel and coincides with the x axis, and soon after that it reflects off the polygon facet and propagates along the x axis when the polygon is at neutral position. In this case, if a scan lens is used, then the incident ray cannot pass beyond the edge of the scan lens housing to reach the polygon mirrors.
2. $x_0 = R_T$: The scan field is symmetric about the z axis, as shown in Fig. 3.7. However, the incident ray is tangent to the edge of the scan lens and may not be able to pass beyond the lens housing.

In summary, analysis under the conditions of $\psi = 0$ and $x_0 = R_T$ reveals that a symmetric scan field distribution may be produced by rotating a prismatic polygon with special arrangements. However, this may not be possible due to practical considerations.

3.2.4 Effect of vignetting and scan duty cycle

A light ray is a geometrical concept, and in reality, we can only deal with light beams. Light beams with circular or elliptical cross-sections are commonly

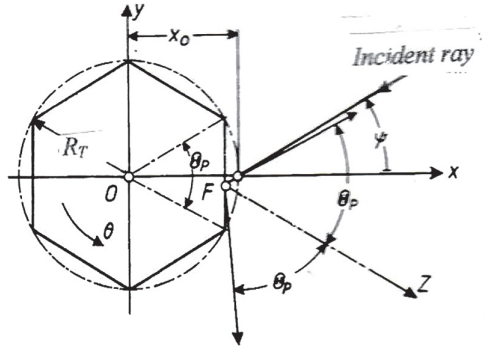

Figure 3.7 Cross-sectional view of a polygon scanner showing the symmetrical structure of scan field produced under the condition of $x_0 = R_T$.

Characterization parameters of the scan field produced by regular scanners of $M = 4$ to 20 are computed and the results are listed in Table 3.1 given a total beam scan angle of $2\Theta_p$. However, considering the effects of vignetting and the facet clear aperture, the active scan angle Θ_a is only (50−60)% of Θ_p, and the total active scan angle $2\Theta_a \cong (1.1 - 1.2)\ \Theta_p$. Under this condition, the characterization parameters of the scan field produced by regular scanners of $M = 4$ to 20 are computed and the results are listed in Table 3.2.

Comparing the numerical results listed in Tables 3.1 and 3.2, the following information needs our attention:

- The angular separation γ between the ray of incidence and the up-reflected ray is an essential parameter to permit the ray to pass beyond the edge of the scan lens housing, and $\gamma < 0$ means that either the scanning ray is unable to pass beyond the edge of the scan lens housing or that a scan lens is not acceptable by the system. In Table 3.1, we see $\gamma < 0$ for most of the cases, whereas Table 3.2 shows $\gamma > 0$ for most cases.
- The last column of Table 3.2 shows the percentage reduction of DF/R_F as compared with the values of DF/R_F listed Table 3.1. On average, the total reduction is 54.9%.

3.3.3 Scanning with a convergent beam and the locus of its focal point

Polygon scanning with a convergent beam is a frequently encountered task for post-objective scanning, as discussed in Appendix C. [1.11]

A convergent beam has a focal point, known as the ray of congruence in geometrical optics, which moves with beam steering. This subsection considers the locus of the moving focal point when a polygon rotates, which is a necessary step for evaluating the distortion of a scanning spot on the observation plane due to defocus of the scanning beam.

Figure 3.20 shows that the focus of the convergent beam moves along a curve in the space. In order to estimate the defocus, i.e., the difference of this curve from an ideal circular curve, one must know the curvature of the scan field.

Figure 3.20 shows that the incident beam converges to the point G specified by (x_g, y_g), for which the mirror image of point G is located at the point G' specified by

$$x'_g = x_g - 2d\cos\theta,\ y'_g = y_g - 2d\sin\theta. \tag{3.40a}$$

Here, $d = x_g\cos\theta + y_g\sin\theta - R_F$ is the perpendicular distance from the point G to the surface of polygon facet being illuminated. The Cartesian form of

Chapter 4
Differential Geometry of the Ruled Surfaces Optically Produced by Mirror Scanning Devices

Ruled surfaces, also known as scrolls, are the surfaces built up by moving a straight line along a certain course in the 3D Euclidean space (E^3). Many geometers have studied ruled surfaces for centuries to gain rational knowledge about how the surfaces in E^3 are generated, and their findings are now essential in all monographs on differential geometry. In the area of optical scanning, scan fields produced by mirror scanning devices of different configurations are surfaces with a light ray as its generating element [4.1–4.3]. This implies, within the accuracy of geometrical optics, that all scan fields are ruled surfaces by nature, and the theory of ruled surfaces in differential geometry provides a land with precious deposits for structural analysis of the scan fields.

The rectilinear propagation of light rays in the homogeneous isotropic media makes it possible for the optical generation of ruled surfaces as the ray is deflected by a rotatable mirror. Scan patterns on a plane or on a curved surface are merely curves on the ruled surface. Based on this understanding, structures of the scan fields produced by mirror scanning devices of different configurations may be classified as the ruled surfaces of different orders in the frame of differential geometry. [4.4–4.7]

This chapter has two phases: phase one has four sections for the analysis and classification of the ruled surfaces produced by mirror scanning devices of different configurations and phase two has two sections for ruled surfaces produced by multi-mirror-scanning systems.

In the first section, general expression of the scan fields produced by mirror scanning devices is re-written in the form properly normalized and parameterized to conform with the definition mode of a ruled surface in

4.2.2 Ruled surface produced by a Galvanometric scanner

The mirror of a Galvanometric scanner under the illumination of the ray of incidence specified by two parameters sketched in Fig. 4.5(a) that is different from the one parameter arrangement shown previously in Fig. 2.16(b). The configuration shown in Fig. 4.5(a) may be regarded as a single-facet prismatic polygon with the mirror mounted against axis of rotation, i.e., $x_0 = 0$ for the mirror in Fig. 4.1. In addition to the change in mirror mounting, the mirror motion is also changed from the mode of a continuous rotation into an oscillation.

By ignoring all of the terms containing x_0 in Eq. (4.22), we may obtain the Cartesian expression for the ruled surface produced by a Galvanometric scanner in the form

$$(z - z_0)^2 \tan^2\varphi - (x^2 + y^2) + y_0^2 = 0. \tag{4.18}$$

In consideration of the standard form of a second-order (i.e., quadric) surface, we may express Eq. (4.18) more explicitly as

$$\frac{x^2}{(y_0 \tan\varphi)^2} + \frac{y^2}{(y_0 \tan\varphi)^2} - \frac{(z - z_0)^2}{y_0^2} = 1. \tag{4.19}$$

The surface described by Eq. (4.19) is known as the one-sheet hyperboloid of revolution that is one of six typical of quadric surfaces. Sections made by planes, which are in parallel with the z axis of one-sheet hyperboloid of revolution, are hyperbolas, and by the planes perpendicular to the z axis are

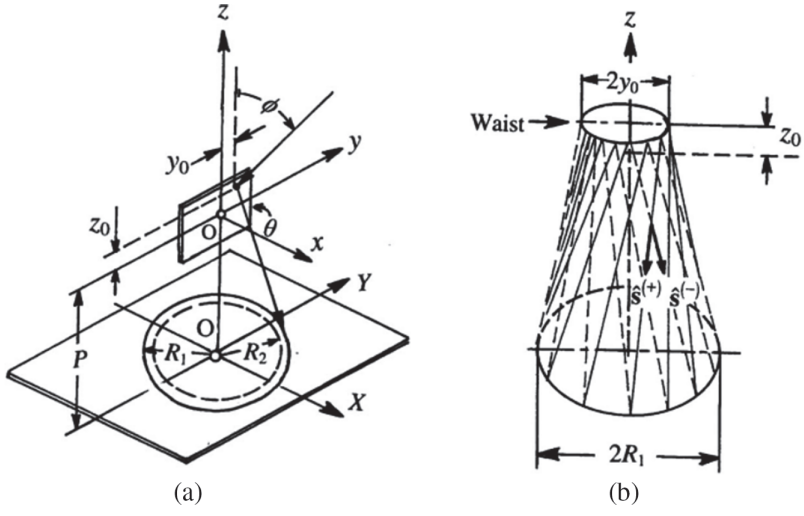

Figure 4.5 Ruled surfaces generated by a Galvanometric scanner: (a) Scanning geometry and illustration of notation; (b) the one-sheet hyperboloid of revolution as a doubly ruled surface.

The process of combining a circular and a linear motion together with a movable straight line about a fixed axis produces a Plücker's conoid, as shown schematically in Fig. 4.2(b). This process can be described by an equation in the form (see, e.g., Eq. (14.9) on p. 436 of Ref. [4.4])

$$\mathbf{r}(\theta, \rho) = d(0, 0, \sin q\theta) + \rho(\cos\theta, \sin\theta, 0), \tag{4.31}$$

where $\mathbf{r}(\theta, \rho)$ is a variable point on the conoid, $\rho = \rho(x, y, z)$, and $2d = \overline{Q_1 Q'_1}$ is the range of moving the line along the axis. Other notation is illustrated graphically in Fig. 4.2(b).

We may repeat the same statement about generation of a Plücker's conoid to describe the development of the optically produced ruled surfaces if the terms "straight line" and "axis" for the Plücker's conoid are replaced by the terms of "deflected ray" and "incident ray", respectively. However, the requirement for perpendicularity between the generator and the base curve of the Plücker's conoid [see $\Phi = \pi/2$ in Fig. 4.2(b)] cannot be met by the optically produced ruled surfaces under almost all circumstances except the special case illustrated in Fig. 4.9(a), in which one half of the Plücker's conoid of the one fold optically produced by a monogon scanner with a mirror inclined at 45° relative to the axis of rotation, the ray of incidence is parallel with that axis but displaced from it by a distance of x_0. This arrangement specifies a scanning geometry that ensures the perpendicularity between a line segment on the ray of incidence (i.e., the base curve of the ruled surface) and the ray of reflection (i.e., the generator of the ruled surface), as specified in Subsection 2.1.3.

It is worth of noting that only a portion of the Plücker's conoid defined in differential geometry that can be optically generated due mainly to the incident and the reflected light rays that are half-lines their with endpoints on the base curve. Moving a light ray can create, at the most, one-half of the ruled surface defined in differential geometry of surfaces. Creating and scanning an infinitely long line is an issue to consided in the remaining part of this chapter.

4.4 Optically Creation of Helicoids, Conoids and Hyperbolic Paraboloids by Scanning an Infinitely Long Line

This Section starts with a device that generates a long straight line together with an axis of rotation. After that is a structural comparison of the rule surfaces swept out by a line and by a ray followed by the applications of this device to the optically generated ruled surfaces, such as the helicoids, conoids and hyperbolic paraboloids.

4.4.1 Optical creation of a scanning infinitely long line

A line, as a geometrical object, is straight, infinitely long, and infinitely thin, whereas a ray is a portion of a line that begins at one point (source) and goes

Chapter 5
Two-Mirror and Two-Axis Scanning Systems of Different Configurations

The two-mirror/two-axis laser beam scanner to be considered in this chapter contains two single-mirror/single-axis scanners which scan along the X- and the Y-directions, respectively, to produce 2D scan patterns of different shapes, such as the sawtooth, or the triangle and the raster patterns... etc. The two-mirror/two-axis laser beam scanners are therefore also known as the XY scanners.

An analytical model is developed to predict the structures of the scan fields generated by the XY scanning systems of three different configurations:

- Two Galvanometric scanners in cascade (i.e, the G-G system for brevity),
- A paddle scanner and a Galvanometric scanner in cascade (i.e., the P-G system),
- The golf club scanner and a Galvanometric scanner in cascade (i.e., the G-C system, or the golf club 2D scanner).

Comparing to the G-G system, the P-G and G-C systems may be regarded as the improved designs to achieve the so-called single-origin-XY-scanning to overcome some unfavorable effects introduced by the astigmatism distortion in the scan field produced by G-G system, as will be seen in the subsequent discussion. It is also worthy of mentioning that the scan field generated by the three systems can be divided into the near- and the far-field regions, in which the scan pattern depends strongly on the system configuration only in the near-field region. This situation opens a way to develop a unified approach for structural analysis of scan fields in the far-field region, where we may examine the optical distortions in the scan patterns at the pixel level regardless to the differences in the configurations of their producer.

parallel to the yz-plane. The rotation axis of the mirror is perpendicular at the point of ($y = d$, $z = h$) on the arm. The second mirror M_2 is driven by a galvanometer and rotates about the axis in the mirror plane that is perpendicular to the xz-plane, which implies the axes of the two mirrors are, respectively, parallel to the x- and the y-axes, i.e., they are parallel in 3D space but not intersect at a point. The two mirrors are all in rotational motion specified by the angles of rotation

$$\theta_1 = \theta_{10} + \Delta\theta_1 \quad \text{and} \quad \theta_2 = \theta_{20} + \Delta\theta_2, \tag{5.1}$$

where θ_{10} and θ_{20} are the time-independent angles related to the positions when the two mirrors at rest, $\Delta\theta_1$ and $\Delta\theta_2$ are the time-dependent angles, and $(0, 0) \leq (\Delta\theta_1, \Delta\theta_2) \leq (\Theta_{1m}, \Theta_{2m})$, where Θ_{1m}, and Θ_{2m} represent the amplitudes of angular motions of mirrors M_1 and M_2.

5.2 Scan patterns Produces by *XY* scanning systems

The ray path through the model scanner is shown in Fig. 5.2, and the scan pattern on the screen is the solution of mirror-and-ray intersection equation [see Eq. (1.9) in subsection 1.2.3], from which we found scan pattern expressible parametrically in the form

$$X = \left(\frac{P}{\cos 2\Delta\theta_2} - h + d\tan\Delta\theta_1\right)\tan 2\Delta\theta_1 + 2q\frac{\sin\theta_{10} - \sin(\theta_{10} - \Delta\theta_1)}{\cos 2\Delta\theta_1} \tag{5.2a}$$

and

$$Y = -P\tan 2\Delta\theta_2, \tag{5.2b}$$

where we have assumed, when the two mirrors are at their rest positions, the display screen is perpendicular to the scan vector **R** and located at a distance P away from the center of the mirror M_2, as described graphically in Fig. 5.2. It is worth of noting the important prediction of Eqs. (5.2a) and (5.2b) that the center of scan pattern is located at ($X = 0$, $Y = 0$) when $\Delta\theta_1 = \Delta\theta_2 = 0$ regardless to the changes of P, d and q.

5.2.1 *XY* scan patterns produced by systems in different configurations

Since the three configurations described graphically in Fig. 5.1 are the special cases of the generalized model scanner, so we may express the XY scan patterns produced by three different systems from Eqs. (5.2a) and (5.2b) by comparing the scanning geometry shown Fig. 5.1 and 5.2.

flexibility in adjustment of the size focused spots as well as the curvature of the display screen, which remain in focus as the sweep over either flat or curved surface.

The two-lens system is separated from Fig. 5.8(b) and enlarged in Fig. 5.9 to show how optics works for in three-axis (i.e., XYZ) scanning. The lens L_2 is a movable concave lens illuminated by a flat-top beam [5.8], which is expanded into a pencil of rays from focal point F, a point movable at the same time with lens L_2 and plays the role of the object point of focusing lens L_1. The ray-pencil from F is focused by L_1 and converged to the focal point F', that is movable at the same time with the lens L_2 in a different rate. Figure 5.9(b) shows that when L_2 moves closer to L_1, the image distance increases, i.e., the image point F' scans points on the z-axis as predicted by geometrical optics.

5.5 Software Correction of Distortions in Digital Images Produced by Two-Mirror and Two-Axis Scanners

It is known from previous Chapters that a scan pattern can be drawn on the plane of observation if the control laws of mirror motion are given. Regretfully, the drawn pattern is usually an approximation to what we desired, because different kind of distortions may come with the pattern. Now we want to know the desirable control laws for mirror motion, which can steer beam to produce the desirable error-free pattern on the same plane.

Further, it is also known that the control law of mirror is a mathematical formula, say $X = F(\theta)$, used by the servo-system to determine the angular position θ of the mirror, and an error-free scan pattern may be produced if we can find the inverse control law, say $\theta = F^{-1}(X)$, to control mirror motion correctly, where X represents the coordinates of the error-free pattern and F^{-1} is the inverse function of F.

The first part of this section is a constructive analysis of F^{-1} from the viewpoint of inverse mapping of F, and the second part is a case example to show the numerical procedure applicable to software correction of distortions in digital images produced by two-mirror and two-axis scanners.

5.5.1 Software correction of scanning errors in digital images

Image formation is a mapping of an object to an image plane. Figure 5.9 provides a simple example about the correspondence between object point F and image point F' in case of a two-lens system.

There are two types of images in ray optics: the real and the virtual images. A real image is formed when light rays pass through and diverge from the image point. Real images can be displayed on screens and may be generated by optical systems such as lenses. A virtual image is formed when light rays do not pass through the image point but only appear to diverge from

Chapter 6
Gimbaled Mirror for Two-Dimensional Beam-Steering

The vector approach to tracing the path of a light beam through an optical system containing movable plane mirrors has been the subject of a number of publications [2.1, 3.1, 3.5, 6.1] as summarized in chapter 1, which provided a basis for modeling scanning systems of different configurations containing one or two mirrors movable about an axis or their respective axes as presented in the preceding Chapters. The present Chapter intends to carry this effort further to an analysis and synthesis of scan patterns generated by a single-mirror beam steering system, in which a gimbaled movable mirror is able to turn about a fixed pivot point and steer optical beam in different directions. In spite of the apparent simplicity of its mechanical arrangement (see Fig. 6.1), the structural analysis of the scan field may be tedious. This is because the mirror has more freedom in angular motion to accomplish XY scanning, which can not be obtained by a single one-mirror and one-axis device.[2.8, 6.2] Another special advantage of gimbaled mirror is scan field produced by a single point source when the ray of incidence hits the center of the gimbaled mirror. Under this condition, no need to divide the scan field into near- and far-regions. Nowadays, gimballed mirrors are the most commonly used beam-steering systems.

To this point, it is worthy of noting that the gimbaled mirror shown in Fig. 6.1 is not a mirror mounted on a ball hinge but a mirror held by a set of two gimbals, one mounted on the other with their axes of rotation lying in one plane and in the perpendicular direction, as detailed in Fig. 6.16 below.

This Chapter is divided into six sections. In Section 6.1, expressions are developed and summarized for scan patterns formed under different conditions; case examples are presented to illustrate the nature of high-order conic-section scan patterns produced by gimbaled mirrors. In Section 6.2, the inversed problem is discussed, i.e., how to control mirror motion to generate the desirable scan patterns. Section 6.3 considers the effect of input offset on the size and orientation of a laser scanning spot with an elliptic cross-section and optical distortions in laser-projection-images composed of square or non-square pixels

of parameter β_0] that mirror vector $\hat{\mathbf{n}}$ sweeps out a cone with the cone angle given by the expression [see, Fig. 6.6(a) for definition of parameter Φ]

$$\Phi = \frac{\pi}{4} - \frac{1}{2}\arccos\left[\frac{1}{\sqrt{1+(m\sin\varphi - y_k\cos\varphi)^2}}\right]. \tag{6.34}$$

As an example, Fig. 6.7(b) shows the raster pattern of $N = 4$, which looks like the character "M" written on the screen, which is also appeared on surface of the unit sphere as the spherical representation of "M".

6.3 Distortions in the Images Produced by Gimbaled Mirrors

The first topic in this section is the effect of input offset on scan pattern, which provides importance information for establishing tolerance budget related to optical assembly of single-mirror beam steering system. We will also show scan-line broadening and pixel deformation in the 2D image display. Another two factors to measure optical distortions, i.e., the SBL and LIN, have been discussed in the previous sections; the computed results are shown in Figs. 6.3(c) and 6.6(c).

6.3.1 Effect of input offset

Figure 6.1 shows the axis of the beam of incidence is parallel to but not coincident with the y axis. The distance between them is specified by the input offset (ξ_0, η_0) that may introduce considerable distortion in the scan pattern when viewed in the near field where the display screen is placed at a distance $P \simeq \sqrt{\xi_0^2 + \eta_0^2}$, whereas a little amount of distortion is seen when an observation made at a distance $P \gg \sqrt{\xi_0^2 + \eta_0^2}$.

The above conclusions were drawn under the basis of the computed results shown in Fig. 6.8 which was plotted from Eq. (T2) in Table 6.1 along with the case example in the Subsection 6.2.3 relating to the generation of a circular pattern.

In Fig. 6.8, effect of input offset is shown by the change of the circularity (roundness) of the two circles of radii $R_0/P = 0.5$ and 1.0 with the increasing values of the relative offset $\xi_0/P = \eta_0/P = 0$, 0.01, 0.05, and 0.1. The dashed line curves in in Fig. 6.8 show the two circles are gradually out of shape, and significant optical distortion is seen when $\xi_0/P = \eta_0/P = 0.1$ which implies either a large offset (ξ_0,η_0) or an observation too close to the mirror. To reduce offset distortion in near field scanning, system alignment accuracy of $\sqrt{\xi_0^2 + \eta_0^2}/P \ll 1\%$ may be required.

A full summary of the performance comparison of the two systems is given in Table 6.3.

Finally, it is interesting of noting that Figs. 6.13 and 6.14 are plotted under the assumption that the pincushion distortions associated with the raster scan patterns have been corrected either by software, or by f-theta flat-field lens. However, some very small pincushion distortions are still seen as indicated by the dashed curves on the two sides of the projection images shown Figs. 6.13(b) and 6.14(b). This finding reveals the existence of a different kind of optical distortions at pixel level, which are uncorrectable due mainly to the fact that they are from an intrinsic characteristic of the law of reflection in optics, not from a man-made control law of mirror motion.

6.7 Gimbaled Mirror and MEMS Micro-Scanners

As mentioned at the beginning of this Chapter that orientation of a gimbaled mirror is determined by two parameters (see, e.g., angles Θ_H and Φ_H below), which implies a mirror with two scan axes. Such a device has been invented two hundred years before the invention of laser beams for the purpose of reflecting sun light to a fixed target and since then it was known as a heliostat in literatures, because of its ability to trace the sun's apparent motions in the sky. [6.9].

Table 6.3 Comparison of performance of systems of different configurations.

Item	Single-mirrow system	Two-mirror/two-axis system	Comments
System configuration	A hinged movable mirror turning about a fixed pivot point.	Two mirrors rotating around their respective axes in orthogonal direction.	
Aagular motion of the mirror(s)	The maximum mirror deflection angle Φ_m in any direction	Amplitudes of mirror tatation angles $\Theta_{1m} \times \Theta_{2m}$	$\Phi_m \approx \Theta_{1m} + \Theta_{2m}$ Two-mirror/two-axis system has smaller amplitudes of mirror angular motion.
Image in the near-and far-field regions	Image aspect ratio remains unchanged in the near- and far-field regions.	Image aspect ratio is different in the two regions.	See Ref. 10 for details.
Frame distortion	Double pincushion distortion.	Pincushin distortion.	Can be corrected by modulation of mirror motion function. See Ref. 10 for details.
Type of pixel distortions	Rhombic distortion.	Parallelogram distortion.	Pixel size changes and rotaion.
Image resolution	• Higher resolution in the center and lower resolution in the corners. • Two-mirror/two-axis system may provide a higher resolution.		See numerical examples in Figs. 6 and 7.

Chapter 7
Exact and Approximate Solutions for Risley-Prism-Based Beam-Steering Systems in Different Configurations

Risley prisms are pairs of rotatable prisms that can be used to continuously scan a laser beam over a wide angular range with a high resolution. Risley prisms are particularly useful in optical tracking and pointing a target in free space

Chapters 7 through 10 are the four Chapters in Part III of this book and devoted to a discussion of Risley-prism-based beam-steering systems (i.e., rotating wedge prism scanning systems), which have two basic problems in practical application. Chapter 7 considers the exact and approximate solutions of first problem, i.e., given the two prisms' orientations, in what direction does the laser beam propagate after emerging from the system? Chapters 8 and 9 consider the second problem, which may be regarded as the inverse of the first one, i.e., given the required pointing position, what will be the orientations of the prisms? Prism systems in these three Chapters are considered error-free: no prism tilt and no beam and mechanical axes misalignment, which will be considered in Chapter 10 of this book.

Optical Prisms are ideal for ray deviation. Refractive prism (the "prism" for short) is one type of the optical prisms for redirecting light at a designated angle. [7.1] Refractive prisms for steering optical beams are usually the wedge-type prisms, whose principal section is a right triangle and can be divided into three types according to degrees of their opening angle (see, e.g., Fig. 7.1).

- The wedge prism is a prism with a shallow wedge angle that is a few degrees, for which the first-order approximation may predict results with sufficient accuracy in some applications. [7.2] Wedge prisms are used in Risley prism pointer for high speed pointing and tracking of remote target.

Chapter 8
Forward and Inverse Solutions for Two-Element Risley-Prism-Based Beam-Steering Systems in Different Configurations

There are two basic problems regarding applications of Risley-prism-based beam-steering systems for directing a laser beam to illuminate a point of interest. First, given the two prisms' orientations, in what direction does the laser beam propagate after emerging from the system? The second problem may be regarded as the inverse of the first one, i.e., given the required pointing position, what will be the orientations of the prisms? The answer to the first problem can be found in a number of publications [7.9, 7.18, 7.19, 7.25] as summarized in Chapter 7. Investigations of the second problem, which is known as the inverse problem or the problem of precise pointing [7.9, 8.1–8.4], have been stimulated by the applications of Risley prism pairs to optical tracking and pointing at targets in free space.

Solutions for the inverse problem, which can be regarded as exact, are very rare in the literature. Historically, Amirault and DiMarzio found in their 1985 paper [8.1] some difficulties in inverting the vector equations for refraction at the surfaces of the prisms for an exact solution to the problem of precise pointing using Risley prism pairs. However, they proposed a realistic approach to obtain an inverse solution through a two-step method, which will be specified in this chapter. Ten years later, Boisset and Robertson et al. [8.2] proposed a paraxial method and developed an iterative algorithm to solve the inverse problem. Furthermore, Degnan [8.3] developed in 2002 a first-order approximation method that does not need an iterative algorithm to find prisms' orientations for a given pointing position. Recently, Li proposed a third-order solution for the inverse problem [7.9]. The first exact solution was given in 2008 by Yang [8.4], who investigated the case of a Risley prism pair having two identical dispersive prisms, i.e., prisms whose principal cross

Chapter 9
Inverse Solutions for Three-Element Risley-Prism-Based Beam-Steering Systems in Different Configurations

Application of Risley prism pair for precise pointing a fixed point may be extended to optical tracking a moving target if a third prism is added to eliminate some of the adverse effect arisen from the blind zone and control singularity, which are inherent issues near both the central axis and the edge of the field-of-regard (abbreviated FOR) produced by matched Risley prism pair. [7.4, 7.5, 9.1]

It should not be confused FOR with the FOV (field of view) that is the angular cone perceivable by the sensor at a particular time instant in moving a sensor in a sensing system. FOR is the total area that a sensing system can perceive, in which the sensor is movable. FOV is usually much smaller than FOR, whose axis is known as the boresight. For a stationary sensor, the FOR and FOV coincide. Furthermore, the terms "field of view" and "field of regard" are common nouns, not for a specific optical instrument. For Risley prisms, FOV means the angular cone formed by the beam been steering by the Risley prism pair. In this way, one may say that Risley prism can be used to move the FOV to realize wide-area pointing or to perform tracking a target within FOR.

It is worth of noting that the use of a third prism is not indisputable because it makes the three-element system under-constrained (i.e., more free parameter than unknowns) and, as a consequence, there exists an infinite number of solutions for the orientations of the three refractive elements, because of the trajectory of the moving target can be described by two time-dependent parameters (Φ, Θ), which are not possible to determine three unknowns, i.e., the angular positions (θ_1, θ_2, θ_3) of the three rotating prisms. An additional condition is therefore necessary for a unique solution.

Chapter 10
Error Sources and Their Influence on the Performance of Risley-Prism-Based Beam Steering Systems

This chapter presents analytical and numerical results to elucidate the influence of error sources on the performance of two-element Risley-prism-based beam-steering systems. Different types of error sources are considered, e.g., two prisms with slightly different characterization parameters, such as the difference in their rates of rotation, in their ray deviation power... etc. Analyses are started within the accuracy of first-order approximation because of the need of qualitative data to estimate the dependence of scan pattern distortion on error sources within the scope of first-order approximation; the third-order theory or exact solution will be followed when more details about the effect of the error source are needed, such as the effect of components misalignment (either a tilted prism or a tilted bearing) on the accuracy of laser beam pointing by Risley-prism-based beam-steering systems.

Case examples are given to show the difference between the distorted patterns and the patterns produced by a pair of perfectly identical wedge-prism elements. Furthermore, non-paraxial ray tracing is performed to investigate the effect of assembly errors on the accuracy of beam steering. We found that a misalignment in a bearing axis of rotation with respect to the system optical axis results in a change of beam deflection off the optical axis and causes a severe decrease of pointing accuracy to a level well below that can be reached by a tilted prism.

In this Chapter, attention will be focused on Risley prism pair in the A-1 configuration [see Fig. 7.7(a)], results obtained for A-1 may be readily extended to the A-2, B-1 and B-2 configurations without any changes under the condition of the first-order approximation [see, e.g., Section 10.1]. However, we may use their expressions listed in Tables 7.3 and 7.4 for

If the two elements have slightly different power of ray deflection, that is, the parameter q in Eq. (10.2) is close to but not equal to 1, then in the case of line scan without an initial phase shift (i.e., $m = -1$ and $\theta_{10} = \theta_{20} = 0$), we obtain from Eq. (10.3) an ellipse, given by

$$\frac{X^2}{(1+q)^2} + \frac{Y^2}{(1-q)^2} = (P\delta_1)^2, \tag{10.6}$$

as shown in Fig. 10.3(b).

10.2 Effect of Prism Assembly Errors on Pointing Accuracy of Risley Prism Pointer

Figure 10.4 shows the opto-mechanical arrangement of a two-element Risley-prism beam-steering system, in which the key elements of the system are the two wedge prisms, two hollow-core brushless motors, two sets of bearings, two rotary encoders and a housing that defines a mechanical frame of reference, i.e., the axis of rotation, in reference of which misalignments are defined.

Apparently, first-order approximation presented in Section 10.1 is not suitable for investigating the effect of prism assembly errors on beam pointing accuracy. However, we hope to continue the formulization established in Section 10.1 in order to maintain a coherent description of the influences error sources on the performance of Risley-prism-based beam steering systems.

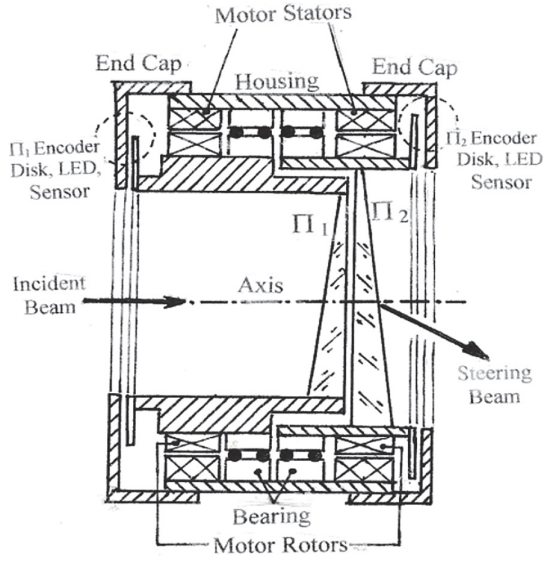

Figure 10.4 Opto-mechanical layout for a Risley prism scanning system in case of using optical rotary encoder in a system in the A-1 configuration.

Yajun Li received his Ph.D. in Electrical Engineering and Computer Science from Pennsylvania State University in 1989 and is an emeritus principal optical engineer from Motorola Solution, Inc. He has published more than one hundred scientific and technical papers in referred professional journals and holds more than 40 U.S. patents in the field of diode laser reliability testing, laser beam shaping, and scanning. He was a member of the editorial board of *Journal of Modern Optics* (formerly *Optica Acta*) from 1982 to 1986 and received a research fellowship from the Alexander von Humboldt Foundation of Germany (1982–1984). He is a fellow of The Optical Society and a fellow of the International Society of Optical Engineering.